Bioelectrochemistry 130 (2019) 107348

Contents lists available at ScienceDirect

Bioelectrochemistry

journal homepage: www.elsevier.com/locate/bioelechem

# High-performance electrochemical enzyme sensor for organophosphate pesticide detection using modified metal-organic framework sensing platforms

Ehsan Mahmoudi [a], Hanieh Fakhri [a], Ali Hajian [b], Abbas Afkhami [c], Hasan Bagheri [a,*]

[a] Chemical Injuries Research Center, Systems Biology and Poisonings Institute, Baqiyatallah University of Medical Sciences, Tehran, Iran
[b] Institute of Sensor and Actuatwor Systems, TU Wien, 1040 Vienna, Austria
[c] Faculty of Chemistry, Bu-Ali Sina University, Hamedan, Iran

ARTICLE INFO

*Article history:*
Received 24 April 2019
Received in revised form 7 August 2019
Accepted 8 August 2019
Available online 9 August 2019

*Keywords:*
Electrochemical biosensor
Metal-organic framework
AChE immobilization
Enzyme inhibition
Paraoxon

ABSTRACT

A practical electrochemical biosensor with high sensitivity was developed for detecting organophosphorus (OP). Initially, Ce metal was introduced into an UiO-66-template to form Ce/UiO-66. Later, graphene oxide (GO), carbon black (CB) and multi-walled carbon nanotubes (MWCNTs) were separately added to Ce/UiO-66 to compare the effect of different carbon-based material types on the performance of the biosensor. Exclusively, Ce/UiO-66/MWCNTs with a Ce (7%) and MWCNT (30%) matrix was found to not only load more acetylcholinesterase (AChE) onto vacant sites but also increase electron transfer and decrease the number of diffusion pathways between the thiocholine and electrode surface. Moreover, the appropriate oxophilicity of Ce coupled with the high surface area and good conductivity of MWCNTs in the UiO-66 structure revealed a high affinity to acetylthiocholine chloride (ATCl) and possible catalysis of the hydrolysis of ATCl with a Michaelis-Menten constant of 0.258 mM. This biosensor, under optimal conditions, demonstrated a rapid and sensitive detection of paraoxon over a wide linear range of 0.01–150 nM, with a low detection limit of 0.004 nM. As a result, the AChE/Ce/UiO-66/MWCNTs/GCE biosensor can be employed in laboratory and field experiments to determine paraoxon levels.



## 1. Introduction

Organophosphorus compounds (OPs) are extensively used in agriculture as pest controllers (e.g., malathion, paraoxon, diazinon), nerve agents (e.g., sarin, soman, tabun and VX) and flame retardants [1,2]. Tremendous residual quantities of waste OPs have been detected in air, soil, water and agricultural products such as fruits, vegetables and crops [3,4]. Public health organizations are concerned about the existence of OPs in the environment and human body due to the high toxicity of these compounds. Exposure to OPs may result from inhalation, drinking or skin contact [5]. As one of the main AChE inhibitors, OPs cause the accumulation of acetylcholine (ACh) in the human body, which leads to stimulation of the nervous system, muscles and glands [6]. The side effects of exposure to OPs have been severely related to the exposure time and dose [7]. Generally, cardiovascular diseases, asthma, dizziness, immunotoxicity, gastrointestinal disorders, nausea, impaired neurobehavioral functioning, cancer and reproduction ability reduction in men and even death have been reported for OP poisoning [8–10].

With this background, different analytical methods have been employed for detecting OPs such as colorimetric detection [11], fluorescent determination [12], immunoassays [13], gas chromatography [14], gas chromatography coupled with mass spectrometry [15], high-performance liquid chromatography (HPLC) [16], mass spectrometry [17], chemiluminescence detection [18], Enzyme-linked immunosorbent assay (ELISA) [19], capillary electrophoresis [20] and molecular imprinting [21]. Although these analytical techniques have revealed reliable and sensitive results, some limitations exist in their application such as non-portable laboratory instrumentation, sophisticated and valuable equipment, requirement of high-skilled operators, sample pretreatment and time-consuming processes [22,23]. Thus, it is essential to introduce a fast and effective method for determination of OPs.

Recently, electrochemical biosensors have attracted increasing attention due to appropriate sensitivity and selectivity, fast response, time-saving processes, user-friendly procedures, portable feasibility and low cost [24,25]. The selectivity and sensitivity are critical issues to consider in optimizing the performance and utility of electrochemical biosensors. Different enzymes as specific recognition elements are employed for manufacturing biosensors including acetylcholinesterase (AChE), butyrylcholinesterase (BChE), laccase and tyrosinase. AChE is the gold standard bioreceptor enzyme for the detection of OPs. Electrochemical biosensors based on the AChE enzyme have been applied as a highly sensitive surface for OP detection, which can hydrolyze

* Corresponding author.
*E-mail address:* h.bagheri@bmsu.ac.ir (H. Bagheri).

https://doi.org/10.1016/j.bioelechem.2019.107348
1567-5394/

acetylthiocholine chloride (ATCl) to produce thiocholine [26]. Oxidation of thiocholine, which is an electroactive species, results in an irreversible peak. After the inhibition of AChE by Ops, the activity of AChE reduces, leading to a reduced thiocholine peak current. Consequently, measurement of the oxidation peak of thiocholine can play the role of a marker for determining the concentration of OPs. Generally, amperometric acetylcholinesterase (AChE) biosensors offer the best method, even if electroactive species can interfere in the measurement. Additionally, these biosensors are quite sensitive and more suited for mass production than potentiometric biosensors, which have lower detection limits.

In recent years, metal-organic frameworks (MOFs) have been introduced as a new class of porous materials in electrochemical applications. These nanomaterials are constructed from organic linkers with various functional groups and inorganic nodes. MOFs have attracted interest from researchers because of their superior characteristics such as tunable texture, high surface area and high reactivity [27]. MOFs can be used as an ideal loading substrate to immobilize receptors or probes due to the ordered and stable crystalline pores. Despite the attractive properties of MOFs, which present them as ideal materials for the surface modification of electrodes, the signal transduction is a major challenge for MOF-based electrochemical sensors or biosensors [28]. To overcome these problems, including the conductivity and design of redox-active, MOFs are combined with conductive materials to gain satisfactory properties for applications in electrochemical sensors. Furthermore, the high porosity of MOFs can induce a nonnative conductivity by their combination with a variety of functional materials such as metal nanoparticles, carbon nanostructures, polymers, and biomolecules [27,28]. Zhang et al. [29] reported enhanced electrochemical behavior via the fabrication of Ni-MOF/carbon nanotubes. This composite was used as a sensitive non-enzymatic glucose sensor and indicated a low detection limit and a wide linear range. In another study, a Cu-MOF/graphene composite was employed for the detection of hydroquinone and catechol in water [30]. Improved electrochemical detection of $H_2O_2$ was achieved using metal nanoparticles encapsulated in the anionic metal-organic frameworks. By using a AgNPs@Y-1, 4-NDC-MOF/ERGO sensor, a linear detection range was obtained from 4 μM to 11,000 μM with a detection limit of 0.18 μM [31].

In 2008, a series of Zr-based MOFs (such as UiO-66, UiO-67 and UiO-68) were synthesized and evaluated for various applications of MOFs [8]. The Zr-based MOFs revealed higher thermal and chemical stability compared with other types of MOFs. Particularly, UiO-66 was widely utilized in electrochemical applications [28,32,33]. However, the redox properties of UiO-66 are restricted owing to the inert nature of $Zr^{4+}$. Thus, the doping of the metal source is a suitable approach to adjust this preferred property [34]. For example, several studies have reported the addition of a second metal in the UiO-66 structure such as $Hf^{4+}$, $Ti^{4+}$and $V^{5+}$ [35–37]. Ce has suitable redox properties between the two valence states of $Ce^{3+}/Ce^{4+}$ and speeds up electron transfer [38,39]. Additionally, as indicated in [40], Ce has a much higher oxophilicity compared with Zr, which improves the immobilization of AChE. On the other hand, the higher oxophilicity increases the affinity and adsorption of ATCl on the biosensor surface, which leads to increased thiocholine production and enhancement of the electrochemical signal [41,42]. To further enhance the electrochemical behavior, Ce/UiO-66 was composited separately with various carbon substrates including graphene oxide (GO), carbon black (CB) and multi-walled carbon nanotubes (MWCNTs). The composites based on MOFs present the advantages of both MOFs and other modified materials (conductivity and catalytic properties), and the electrochemical performances are enhanced [43,44].

In this study, the effects of Ce doping on the UiO-66 structure and the type of carbon nanostructures used as conductive components in an electrochemical biosensor were investigated. The high-performance features of the prepared composite are found to be due to the synergistic combination of both MOFs and MWCNTs. Additionally, the dose of Ce and carbon-based substrate, modifier volume, AChE amount, buffer pH, ATCl concentration and incubation time were all evaluated. We found that AChE/Ce/UiO-66@MWCNTs@GCE is a suitable electrochemical biosensor for the detection of paraoxon.

## 2. Experimental

### 2.1. Materials

Acetylcholinesterase (AChE) from *Electrophorus electricus* (C2888) and acetylthiocholine chloride (ATCl) (A5626) were purchased from the Sigma-Aldrich company. Zirconium tetrachloride ($ZrCl_4$) and cerium trichloride heptachloride ($CeCl_3.7H2O$) were supplied by Sigma-Aldrich and used as Zr and Ce precursors. Dimethylformamide (DMF) and 2-aminoterephthalic acid (NBDC) were supplied from Merck and utilized as synthesis agents. Additionally, carbon black (CB), graphene oxide (GO) and multi-walled carbon nanotubes (MWCNTs) were acquired from Sigma-Aldrich. Sodium phosphate dibasic heptahydrate ($Na_2HPO_4.7H_2O$) and sodium phosphate monobasic monohydrate ($NaH_2PO_4.H_2O$) were purchased from Merck and used for making PBS, with HCl or NaOH used to adjust the solution to the final desired pH. Paraoxon was purchased from Sigma-Aldrich and a 0.01 M stock solution was stored at 4° C. Ultrapure double-distilled water was used in all synthesis procedures. All materials were of analytical grade and used without any further purification.

### 2.2. Apparatus

All electrochemical analyses were performed by a potentiostate/galvanostate (Vertex, Ivium Technologies, Netherlands) workstation with three electrodes. As a current procedure, a modified glassy carbon electrode (GCE) was used as the working electrode, a platinum electrode as the auxiliary electrode and Ag/Ag-Cl electrode as the reference electrode. Scanning electron microscope (SEM) images were taken using a Tescan MIRA3. The XRD patterns for the nanocomposites were detected using a 38,066 Riva, d/G. Via M. Misone, 11/D (TN), using Kα radiation ($\lambda = 1.5418$ A°) with a scanning rate of 2° per minute and 2θ range of 5°-80° with Cu Kα radiation for the determination of the crystalline phase of the samples. The FT-IR analysis was performed using a PerkinElmer spectrometer in the wavenumber range of 4000–400 $cm^{-1}$ using KBr disks.

### 2.3. Synthesis of UiO-66

In the first step, 0.38 g $ZrCl_4$ was dissolved in 20 mL DMF, and then 0.27 g NBDC was added to the solution. In the second step, the mixture was sonicated for 30 min. Then, it was transferred to a Teflon-lined autoclave and heated at 120 °C for 24 h [45]. The sediment was separated by centrifugation and washed with DMF and methanol several times. Finally, the product was dried at 120° C for 36 h.

### 2.4. Synthesis of Ce-doped UiO-66 (Ce/UiO-66)

Typically, a mixture of 0.08 g $CeCl_3.7H_2O$ and the precursor of UiO-66 (0.38 g $ZrCl_4$ and 0.27 g NBDC) were dissolved in 25 ml DMF to form 7% Ce-doped UiO-66. The thermal and purification procedures were similar to the synthesis method used for UiO-66 [46]. This product is labeled as Ce (7%)/UiO-66. Other quantities of dopant were synthesized using the above-mentioned method.

### 2.5. Synthesis of Ce/UiO-66@MWCNTs (Ce/UiO-66@MWCNTs)

In this procedure, 1 g MWCNTs was dispersed in 30 mL DMF, and then sonicated for 50 min. Next, various amounts of $CeCl_3.7H_2O$, 0.38 g $ZrCl_4$ and 0.27 g NBDC were added to the solution. The resulting suspension was stirred for 60 min. Subsequently, it was placed into an

autoclave and maintained at 120° C for 14 h. The Ce/UiO-66@MWCNTs was achieved by washing with methanol and DMF. A filtered precipitate was the final product. Additionally, Ce/UiO-66@GO and Ce/UiO-66@CB nanocomposites were synthesized by using a similar method.

### 2.6. Fabrication of the biosensor

Primarily, the bare GCE was polished with 0.05 alumina powder for the purpose of obtaining a shiny mirror surface look, followed by sonication in ethanol and water for 10 min. Later, the GCE surface was dried by placing it into a pure nitrogen stream. The stock Ce/UiO-66@MWCNTs modifier was sonicated for 10 min, and then 8 μL was drop cast onto a clean GCE surface before letting the modified electrode to dry in ambient conditions. Later, the prepared electrode was coated with 3 μL AChE solution (100 U/mL in PBS pH 7.5) and placed into a refrigerator to incubate for 1 h. Then, the obtained electrode was washed carefully with PBS (pH 7.5) to eliminate the unbound AChE. The fabricated AChE biosensor was named AChE/Ce/UiO-66@MWCNTs/GCE. The other biosensors were also fabricated in a similar way for the purpose of comparison. The prepared biosensor electrode was stored in a sealed container at 4 °C. Different steps for the fabrication and the principles of the AChE biosensor are shown in Scheme 1.

### 2.7. Real sample preparation

A standard addition method was employed to evaluate the performance of the prepared biosensor. Spinach and cabbage were selected as real samples. Firstly, the samples were washed with doubled-distilled water and then dried at room temperature. Then, 3 g of each chopped sample was introduced into 15 mL PBS (0.1 M, pH 7.5). The samples were placed into an ultrasonic bath for 5 min before being centrifuged for 15 min (1500 rpm). Later, a different amount of paraoxon was added into the real samples and the electrochemical response was obtained by the DPV technique. The concentration of the real samples was determined by the calibration curve.

### 2.8. Electrochemical measurements

For the electrochemical measurement of paraoxon, the proposed biosensor was first dipped into PBS containing various concentrations of standard paraoxon solution for 12 min, and then moved to an electrochemical cell containing 0.1 M PBS (pH 7.5) with 1.0 mM ATCl to evaluate the electrochemical response. The inhibition of paraoxon was calculated as follows:

$$\text{Inhibition}\ (\%) = (I_0 - I_1)/I_0 \times 100\% \quad (1)$$

Where $I_0$ is the peak current of ATCl on the biosensor and $I_1$ is the peak current of ATCl on the biosensor after inhibition by paraoxon.

## 3. Results and discussion

### 3.1. Characterization

Fig. 1(a) shows the XRD patterns for the UiO-66, Ce/UiO-66, Ce/UiO-66/MWCNTs and MWCNTs samples. For the UiO-66 sample, all diffraction peaks were consistent with reported and simulated patterns [47]. These diffraction peaks were retained when Ce was doped into UiO-66, although their intensities were significantly reduced. This reduction indicates that the crystal growth of the UiO-66 units is affected by the incorporation of $Ce^{3+}$, which can also be a metallic site binding with an organic linker [48]. For the XRD pattern of the MWCNTs, two broad peaks were observed at $2\theta = 25.7°$ and 43.2° that refer to the (002) and (001) crystalline planes, respectively. This confirmed the presence of graphite crystallites and the amorphous structure of the MWCNTs [49]. After modification of Ce/UiO-66 by MWCNTs, all peaks belonging to Ce/UiO-66 were preserved, which indicated that the introduction of MWCNTs did not disorder the formation of Ce/UiO-66.

FT-IR analysis provides further information about the samples and the interactions between them. In the spectra for UiO-66, the characteristic bands at approximately 400–780 $cm^{-1}$ correspond to the combination of Zr—O modes with OH– and CH– bending vibrations.

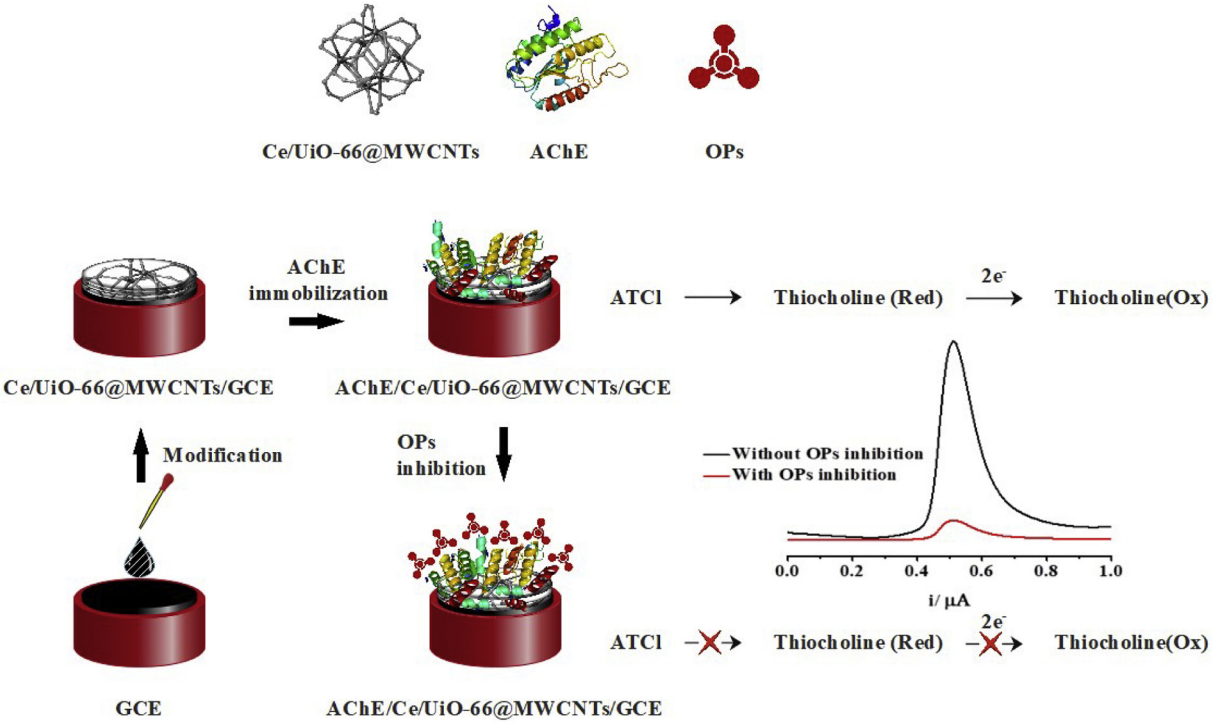


**Scheme 1.** Fabrication steps and principles of the AChE/Ce/UiO-66@MWCNTs/GCE biosensor.

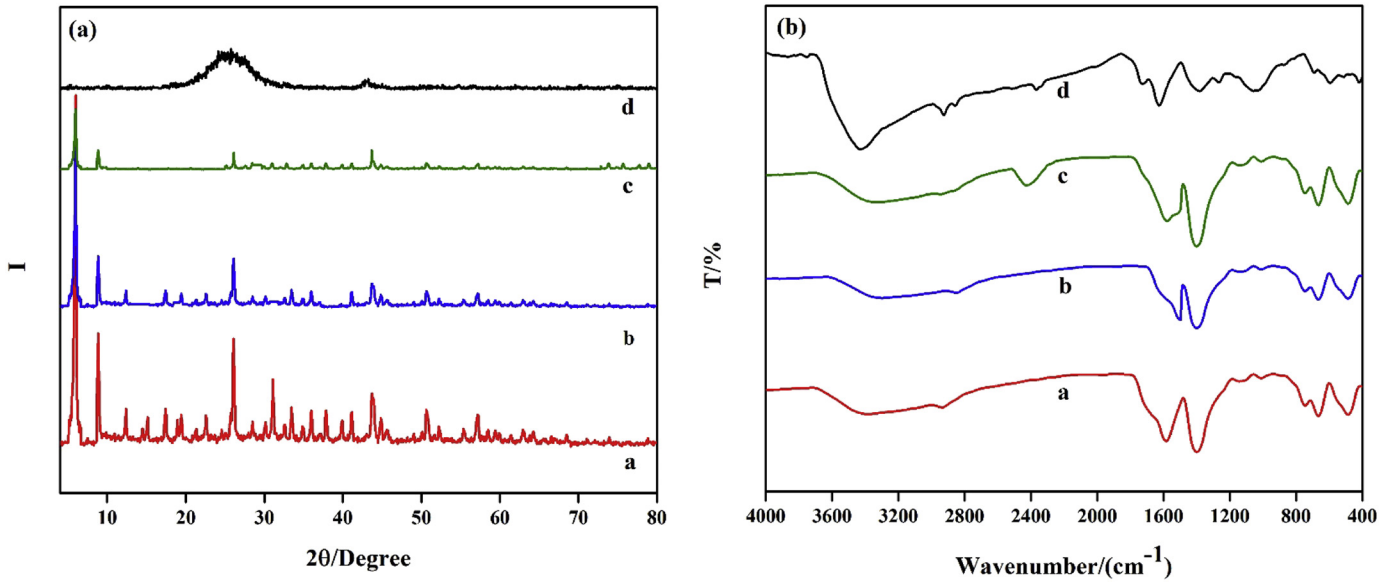


**Fig. 1.** (a) XRD patterns and (b) FT-IR spectra for (a) UiO-66, (b) Ce/UiO-66, (c) Ce/UiO-66/MWCNTs and (d) MWCNTs.

Additionally, the stretching vibrations of C═C and C═O are observed at 1634 and 1710 $cm^{-1}$, respectively [45,50]. After the incorporation of Ce ions, the peak belonging to C═O stretching was altered to a lower frequency, which was attributed to the weaker interaction force of the metal centers. Moreover, Ce—O and Ce-O-C created minor changes at lower wavenumbers [51]. The pure MWCNTs spectra indicated several bands at 3335, 1635, and 1354 $cm^{-1}$, which corresponded to the O—H, C═C and C—O stretching vibrations, respectively. In Fig. 1(b), the new band is placed at 2400 $cm^{-1}$, which corresponds to the interaction of the amine groups in UiO-66 with the MWCNTs [52]. The simultaneous presence of peaks belonging to UiO-66 and MWCNTs confirmed the successful formation of a nanocomposite.

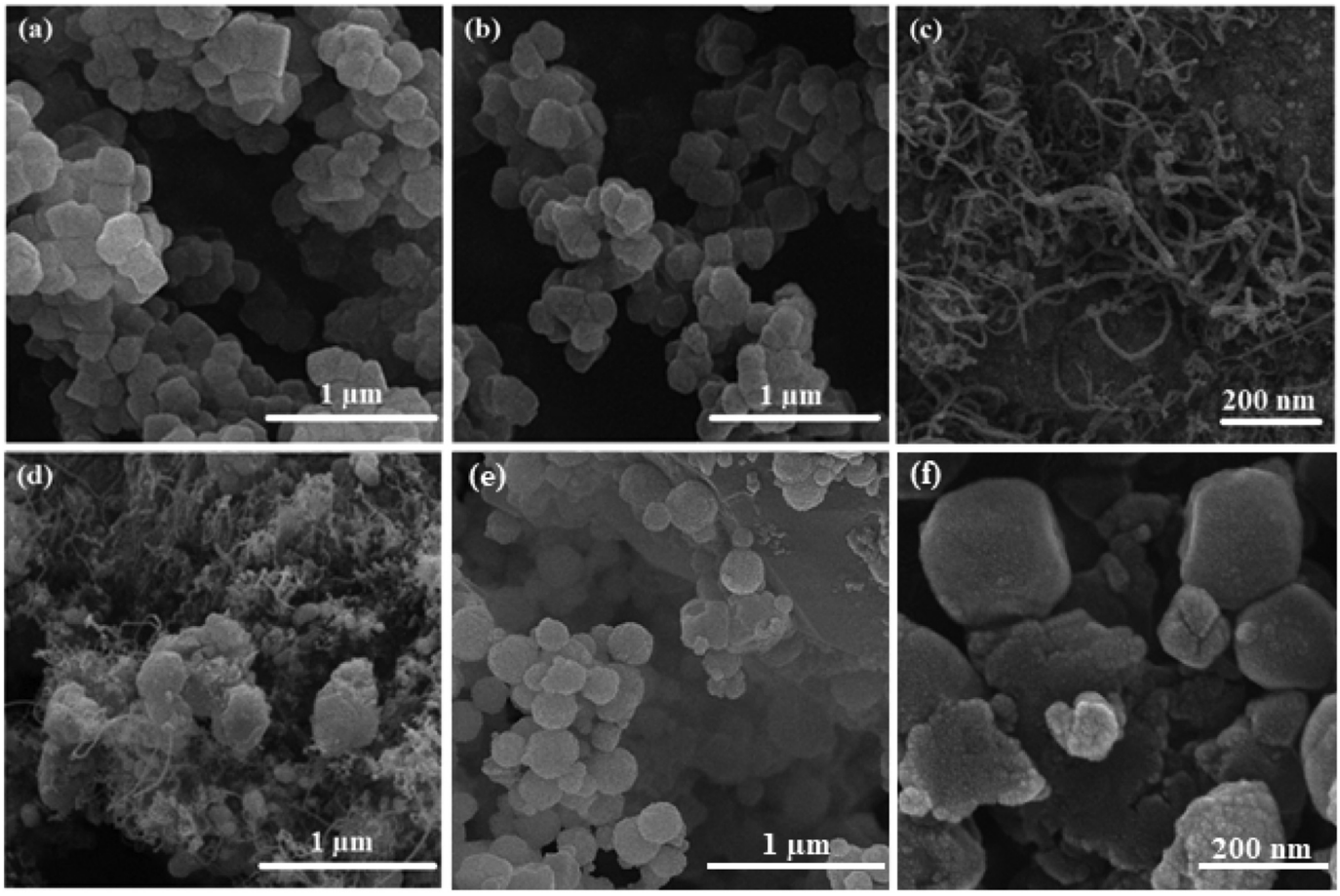


**Fig. 2.** SEM images of (a) UiO-66, (b) Ce/UiO-66, (c) MWCNTs, (d) Ce/UiO-66@MWCNTs, (e) Ce/UiO-66/GO and (f) Ce/UiO-66/CB.

To obtain a clearer insight into the synthesized samples, SEM analysis was utilized. As indicated in Fig. 2(a), pure UiO-66 was observed to show octahedral shapes, which have a uniform size of approximately 150–250 nm. As shown by Fig. 2(b), the entry of Ce particles does not change the morphology of UiO-66. Fig. 2(c) shows the MWCNTs nanoparticles with a size of approximately 25 nm. As seen in Fig. 2(d), a clear boundary is not observed between the MWCNTs particles and UiO-66, which revealed a strong interaction between the two materials. As shown in Fig. 2(e), graphene with its layer structure is coated by Ce/UiO-66 particles, albeit only in some places. For Ce/UiO-66@CB, the simultaneous presence of two composite components is well shown in Fig. 2(f). Therefore, these observations can confirm the results obtained from XRD and FT-IR analyses for the successful synthesis of the nanocomposites.

### 3.2. Electrochemical characterization of the modified electrode

Electrochemical characterization of different electrodes was examined by cyclic voltammetry (CV). Fig. 3(a) shows the CVs for bare GCE, UiO-66/GCE, Ce/UiO-66/GCE, Ce/UiO-66@GO/GCE, Ce/UiO-66@CB/GCE, Ce/UiO-66@MWCNTs/GCE and AChE/Ce/UiO-66@MWCNTs/GCE in 5.0 mM $[Fe(CN)6]^{3-/4-}$ containing 0.1 M KCl. At the bare GCE surface, a pair of redox peaks was observed. After UiO-66 coating onto the GCE, the peak current decreased because of the low conductivity of UiO-66, which blocked electron transfer. Later, a small increment for the redox peaks of Ce/UiO-66/GCE was observed due to the effect of Ce ions in the UiO-66 structure and the redox properties between the two valence states of $Ce^{3+}/Ce^{4+}$. As estimated, after improvement in the Ce/UiO-66/GCE surface with GO, CB and MWCNTs, the currents increased strongly, which is due to the high conductivity of these nanocomposites. Compared with GO and CB, MWCNTs strongly boost the electrical conductivity of Ce/UiO-66/GCE because of their higher conductivity and advanced surface area. Finally, by fabricating AChE/Ce/UiO-66@MWCNTs/GCE, the peak height decreased, caused by poor electron transfer of AChE, which indicates successful immobilization of AChE on the surface of the electrode.

The electrochemical impedance spectroscopy (EIS) for the different electrodes in the probe is shown in Fig. 3(b). The resistance of electron

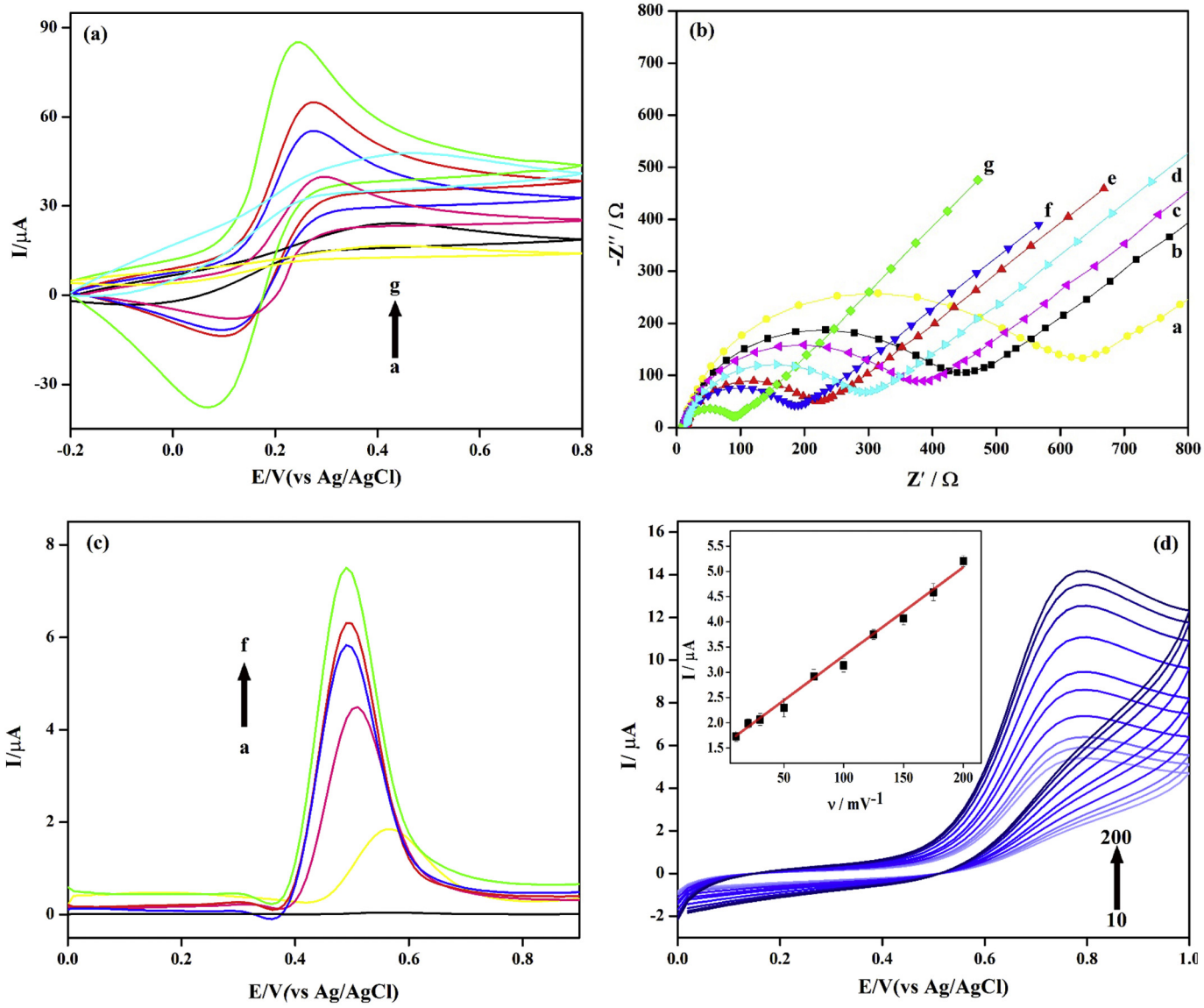


**Fig. 3.** (a) CVs and (b) EIS for (a) UiO-66/GCE, (b) Bare GCE, (c) Ce/UiO-66/GCE, (d) AChE/Ce/UiO-66@MWCNTs/GCE, (e) Ce/UiO-66@GO/GCE, (f) Ce/UiO-66@CB/GCE and (g) Ce/UiO-66@MWCNTs/GCE in $1 \times 10^{-5}$ M $Fe(CN)_6^{3-/4-}$ containing 0.1 M KCl. (c) DPV responses of (a) AChE/GCE, (b) AChE/UiO-66/GCE, (c)AChE/Ce/UiO-66/GCE, (d)AChE/Ce/UiO-66@GO/GCE, (e) AChE/Ce/UiO-66@CB/GCE and (f) AChE/Ce/UiO-66@MWCNTs/GCE in 0.1 M PBS pH 7.5 containing 1.0 mM ATCl. (d) CVs for AChE/Ce/UiO-66@MWCNTs in 0.1 M PBS pH 7.5 containing 1.0 mM ATCl at different scan rates from 10 mV. $s^{-1}$ to 200 mV. $s^{-1}$. Inset: a plot of peak current versus scan rate.

transfer for bare GCE, UiO-66/GCE, Ce/UiO-66/GCE, Ce/UiO-66@GO/GCE, Ce/UiO-66@CB/GCE, Ce/UiO-66@MWCNTs/GCE and AChE/Ce/UiO-66@MWCNTs/GCE was calculated to be approximately 463 Ω, 610 Ω, 380 Ω, 225 Ω, 185 Ω, 85 Ω and 292 Ω, respectively. This implies a tremendous conductivity for the Ce/UiO-66@MWCNTs and the effective immobilization of AChE, which presents the non-conductive nature of AChE.

The DPV peaks for the different electrodes were examined in the absence and presence of ATCl. There were no peaks observed at AChE/Bare, AChE/UiO-66, AChE/Ce/UiO-66, AChE/Ce/UiO-66@GO, AChE/Ce/UiO-66@CB and AChE/Ce/UiO-66@MWCNTs electrodes because of the absence of electroactive species in the electrochemical cell. With the addition of 0.1 mM ATCl to the cell, recognizable peaks were detected on the proposed biosensors, which is due to the oxidation of thiocholine (Fig. 3(c)). Thiocholine is an electroactive species that is produced by the hydrolysis of ATCl catalyzed by AChE. The peak currents increased in the following order: AChE/Ce/UiO-66@MWCNTs > AChE/Ce/UiO-66@CB > AChE/Ce/UiO-66@GO > AChE/Ce/UiO-66 > AChE/UiO-66; There was still no peak detected at AChE/GCE. The best performance was observed for the AChE/Ce/UiO-66@MWCNTs biosensors, which can be justified by the excellent immobilization of AChE, a high surface area and tremendous conductivity.

The effect of the scan rate on the CV of an AChE/Ce/UiO-66@MWCNTs/GCE electrode was studied in 0.1 mM ATCl (Fig. 3(d)). With the scan rate increasing from 10 to 200 mV.s$^{-1}$, the height of the anodic peaks increased. As shown in Fig. 3(d), inset, the peak currents were linearly proportional to the scan rate, which represents a surface-controlled process for this electrode [53]. The AChE has two anionic and cationic sites where the carbonyl site of ATCl binds to a cationic site. After thiocholine production, the nitrogen of thiocholine with positive charge binds to the anionic site of AChE by electrostatic interaction, which justifies the surface-controlled process of this biosensor [54].

### 3.3. Optimization of the biosensor parameters

It is distinguished that the pH of the PBS has a great effect on the biosensor performance. The currents of the biosensor were studied in the range of 6.0 to 9.0, as shown in Fig. 4(a). The maximum value of the current was detected at pH 7.5. Therefore, a PBS with pH 7.5 was selected for further experiments [55]. With the purpose of optimizing the amount of Ce and MWCNTs, biosensors with varying amounts of Ce (from 0% to 11%) and MWCNTs (from 20% to 35%) were proposed and examined under the same conditions. As indicated in Fig. 4(b), 7% Ce and 30% MWCNTs were chosen as optimal amounts due to their higher performance. As revealed in Fig. 4(c), the peak currents strongly improved by increasing the volume of Ce/UiO-66@MWCNTs from 2 to 8 μL, followed by a decrease. In the range of 8–12 μL, increased coating of the modifier onto the surface of the electrode will increase the active site concentration, conductivity and vacant sites for AChE immobilization. However, by further increasing the Ce/UiO-66@MWCNTs volume, the dense and uniformly coated film will stop the electron transfer, which acts as a barrier that prevents thiocholine from diffusing into the interior side of the thick modifier film. Consequently, the appropriate volume of Ce/UiO-66@MWCNTs for drooping was selected to be 8 μL for improving the GCE surface for improving the electrochemical response toward paraoxon detection. The AChE amount played the major role in the biosensor performance. Currents for varying amounts of AChE were investigated in the range of 0.1 U to 0.4 U (Fig. 4(d)). The DPV current increased by increasing the amount of AChE and reached a maximum current at 0.3 U. This was caused by increased AChE immobilization on the Ce/UiO-66@MWCNTs matrix, which fascinated the hydrolyzation of ATCl to thiocholine. Afterward, the DPV current decayed with the addition of AChE due to AChE thickening on the GCE surface, which spoilt the electron transfer. As a result, the optimum AChE amount for the AChE/Ce/UiO-66@MWCNTs/GCE biosensor was considered to be 0.3 U. Additionally, Fig. 4(e) reveals the effect of different ATCl concentrations ranging from 0.1 mM to 1.3 mM on the current in the AChE/Ce/UiO-66@CB/GCE biosensor. The peak currents were apparently amplified when the ATCl concentration was varied from 0.1 mM to 1.0 mM. However, there was no substantial change in current when the concentration was changed from 1.0 mM to 1.3 mM, which is due to the saturation of ATCl on the surface of AChE/Ce/UiO-66@CB/GCE. Therefore, the concentration of ATCl was selected to be 1.0 mM ATCl for this investigation. Incubation time could possibly affect inhibition of biosensors based on AChE. As illustrated in Fig. 4(f), the activity of AChE severely declines with increasing incubation time from 2 min to 12 min. In addition, with a further increase in incubation time, the collaboration between paraoxon and AChE reached saturation and the DPV currents reached a plateau amount where there was no visible change. Thus, an incubation time of 12 min was selected for this study.

Finally, the following optimum parameters were selected for subsequent experiments: pH 7.5 of PBS, Ce (7%) and MWCNTs (30%), 8 μL of AChE/Ce/UiO-66@MWCNTs, 0.3 U of AChE, 1.0 mM ATCl and incubation time of 12 min.

### 3.4. ATCl calibration curve

Fig. 5 illustrates the typical current-time plot for AChE/Ce/UiO-66@MWCNTs/GCE at an applied potential of +0.52 V with successive addition of ATCl under a stirred electrochemical cell containing PBS pH 7.5 solution under optimal conditions. The amperometric response was increased linearly with increasing ATCl to the cell and reached a steady-state current within 5 s after each injection, demonstrating the tremendous catalytic properties of the AChE/Ce/UiO-66@MWCNTs/GCE biosensor. A linear range was obtained from 65 μM to 350 μM. Additionally, the linear equation was calculated using I(μA) = 0.0134C (μM) + 0.2994 ($R$ = 0.9976). The Michaelis–Menten constant ($K_m$), which was evaluated by the Lineweaver–Burke eq. ($1/I_{ss} = K_m/I_{max} \cdot 1/c + 1/I_{max}$), was employed to evaluate the AChE activity toward interaction with ATCl, where $I_{ss}$ is the steady-state current after the injection of the enzyme substrate, $I_{max}$ is the maximum current calculated under a saturated concentration and C is the concentration of the substrate in the electrochemical cell [56]. While the concentration of substrate passed from 350 μM and reached saturation, a plateau was detected; this revealed the kinetics of the Michaelis-Menten model. From the slope of the Lineweaver–Burk equation, the $K_m$ value was calculated to be 0.258 mM, which is expressively lower than the values of 0.43 mM [53], 0.33 mM [57] and 0.7 mM [58] reported by other studies. The smaller $K_m$ of this biosensor indicates that the AChE immobilized on this novel matrix has an advanced affinity to ATCl, possibly as a result of the unique potential of Ce/UiO-66@MWCNTs for AChE adsorption on the electrode surface.

### 3.5. Detection of paraoxon

Inhibition measurements for a varying concentration of paraoxon on AChE/Ce/UiO-66@MWCNTs/GCE were carried out under optimized conditions (Fig. 6). The linear relationship of I (%) = 18.382 log (C/M) + 201.07 ($R$ = 0.9951) (inset a) was calculated for the concentration range of 0.01 nM −150 nM. The limit of detection (LOD) was obtained using the $3S_b/m$ equation, where $S_b$ is the standard deviation of the intercept and m is the slope of the first calibration curve. As a result, the LOD was calculated to be 0.004 μM. According to the end results, the proposed AChE/Ce/UiO-66@MWCNTs biosensor showed an acceptable range of detection and low LOD for the electrochemical detection of paraoxon. A comparison of AChE/Ce/UiO-66@MWCNTs with other biosensors is presented in Table 1. The results show that the AChE/Ce/UiO-66@MWCNTs was basically and potentially comparable to different

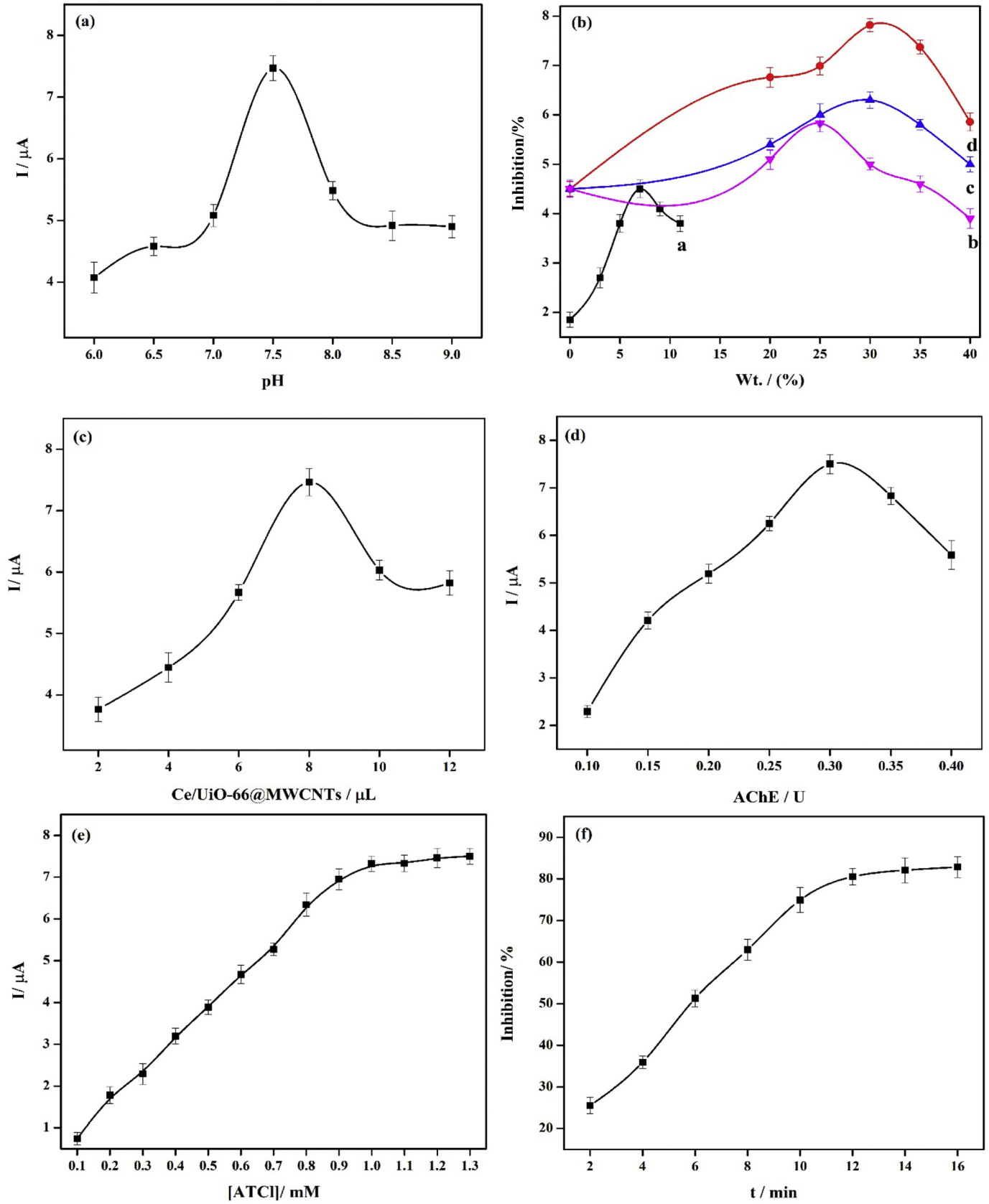


**Fig. 4.** Effect of the (a) pH, (b) Ce and MWCNT wt%, (c) volume of Ce/UiO-66@MWCNTs/GCE, (d) AChE amount, (e) ATCl concentration on DPV respond and (f) incubation time.

biosensors. The novel property of the AChE/Ce/UiO-66@MWCNTs biosensor in terms of electrocatalytic behavior should be attributed to its high electron conductivity, excellent AChE immobilization and large and electroactive surface area. Additionally, compared to the other biosensors, AChE/Ce/UiO-66@MWCNTs was synthesized in an extremely simple and inexpensive way.

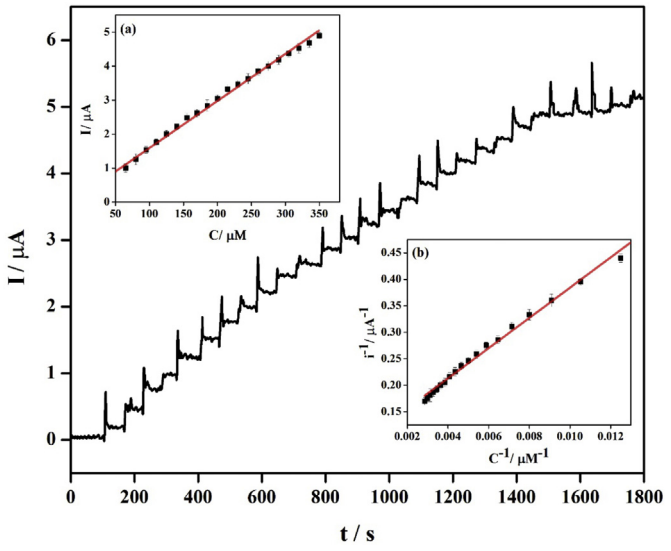


**Fig. 5.** Amperometric I-t plot for the AChE/Ce/UiO-66@MWCNTs/GCE electrode with successive addition of ATCl into 0.1 M PBS pH 7.5. Inset: (a) Relationship between the current and ATCl concentration (b) The Lineweaver–Burk plot of $1/i_s$ vs. 1/C.

### 3.6. Stability, reproducibility and selectivity

The stability property of the proposed biosensor was examined through repeated DPV measurements while the AChE/Ce/UiO-66@MWCNTs/GCE was held at a temperature of 4 °C. It is demonstrated that the biosensor current still remains at 85% of its initial response after 20 days (Fig. 7). These results confirmed the acceptable stability of the AChE/Ce/UiO-66@MWCNTs/GCE. Moreover, the reproducibility was investigated through 5 separately measurements with the DPV technique under constant conditions. The RSD was less than 5% (4.3%), which demonstrates that the AChE/Ce/UiO-66@MWCNTs/GCE presented remarkable reproducibility. Regarding the enzymatic selectivity, the presence of interfering species in a matrix can give rise to a non-enzymatic signal. For example, the oxidation of electroactive species of real samples at an appropriate applied potential leads to an underestimation of the inhibitor amount. Additionally, it is well reported in the literature that enzyme biosensors are characterized by low specificity. In fact, some enzymes are inhibited by a group of inhibitors, for instance AChE is inhibited by different OPs and carbamates. Therefore, in a mixture of these compounds, only an anticholinesterase activity index can be calculated. For interference study, the DPV response in 0.1 M PBS containing 0.1 mM ATCl in the absence (a) and presence of 0.5 mM of oxalic acid(b), 3.5 mM of citric acid (c), 4 mM of glucose (d), 3 mM of $Mg^{2+}$ (e), 4 mM of $Fe^{3+}$ (f), 5 mM of $SO^{2-}$(g), 2.5 mM of $NO^{-}$(h), 10 nM of 4-Nitrophenol (i), 2 nM of carbaryl (j), 2 nM of carbofuran (k), 1.8 nM malathion (l) and 2 nM diazinon (m) was measured after being incubated by 2 nM paraoxon for 12 min, and the results are shown in Fig. 8. The results reveal that no obvious changes in current response are found in the presence of a-h species. However, the constructed biosensor based on enzyme inhibition is not specific: it can be considered as an excellent fast and cost-effective device for methodical screening of OPs. The overall performance indicates that the enzyme sensor shows good reproducibility, selectivity and stability.

**Table 1**
Comparison table of recently fabricated biosesnors for the detection of paraoxon.

| Sensing layer | Linear range (nM) | LOD (nM) | Ref. |
|---|---|---|---|
| AChE/e-GON–MWCNTs/GCE | 0.182–378 | 0.09 | [53] |
| NF/AChE/NF- $Fe_2O_3$@C/CPE | $3.633 \times 10^{-5}$-36.33 | $1.2 \times 10^{-5}$ | [57] |
| Nafion/AChE-CS/Pd@Au NRs /GCE | 0.0036–100 | 0.0036 | [59] |
| NF/AChE/NF-$NiCo_2S_4$/CPE | $3.633 \times 10^{-4}$-0.3633 | $1.3 \times 10^{-4}$ | [60] |
| AChE/AuNRs/GCE | 1–5000 | 0.7 | [61] |
| AChE/Au@Ag NRs/GCE | 5–1000 | 4.3 | [61] |
| AChE/CNT–$NH_2$/GC | 0.2–30 | 0.08 | [62] |
| Poly(FBThF)/f-MNPs/AChE | 0.182–33.71 | 0.079 | [63] |
| PPy-AChE-Geltn-Glut/Pt | 0.3633–545 | 3.9963 | [64] |
| AChE/HGO/GCE | 36.33–163 | 5.74 | [65] |
| SPE/AuNPs/$MoS_2$/GA/AChE+BSA | 3.6–3634 | 0.04 | [66] |
| AChE/N-MALCDs/SPE | $1.8 \times 10^{-5}$-0.36 | $4.8 \times 10^{-6}$ | [67] |
| AChE/Au-MWNTs/GCE | 0.1–7.0 | 1.0 | [68] |
| AChE/Ce/UiO-66@MWCNTs/GCE | 0.01–150 | 0.004 | This work |

### 3.7. Real samples

For the practical detection of paraoxon, cabbage and spinach were selected as real samples. All samples were used without any further purification. Under optimized conditions, samples of varying concentration were spiked into the electrochemical cell. The RSD% for paraoxon in the real sample ranged from 3.2%–4.1%, representing that the AChE/

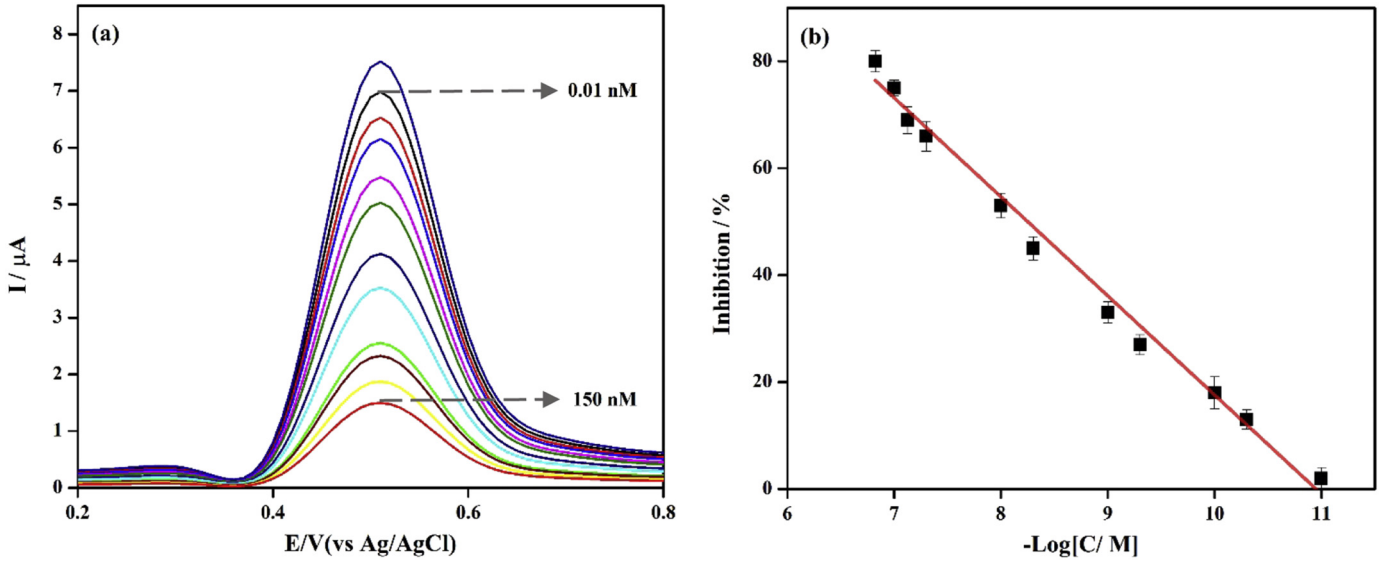


**Fig. 6.** (a) DPV responses for AChE/Ce/UiO-66@MWCNTs in 0.1 M PBS pH 7.5 without and after inhibition with different concentrations of paraoxon for 12 min. (b) The relationship between inhibition rate and paraoxon concentration (I (%) = 18.382 Log [C/ M] + 201.07).

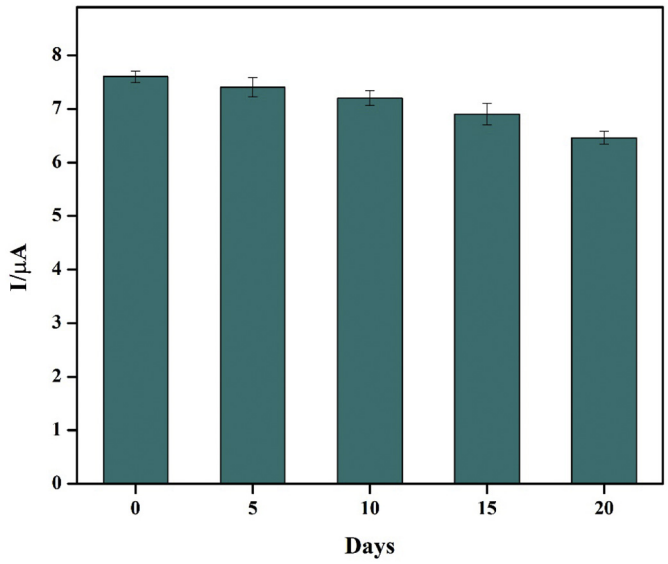


**Fig. 7.** The stability property of the biosensor response measured over 20 days.

Ce/UiO-66@MWCNTs/GCE biosensor had significant potential to detect paraoxon in real samples. The results are shown in Table 2.

## 4. Conclusion

In the fabrication of biosensors, nanomaterials are excellent building blocks that can be used as modifiers of transducers for enhancing their electrochemical signals. Moreover, the development of new functionalized nanomaterials with better and easier immobilization capability for enzymes is still necessary. Therefore, the integration of nanomaterials with MOFs should be further improved from the viewpoint of the sensitivity and selectivity of the resulting enzyme sensors to be used for OPs that can inhibit AChE. Various matrixes aimed at combining the beneficial properties of Ce and carbon-based materials with the UiO-66 structure were fabricated for immobilizing AChE to determine paraoxon concentration. Compared to UiO-66, the proposed matrixes revealed much more acceptable behavior for employment as a host platform for electrochemical enzyme-based biosensors. Ce/UiO-66@MWCNTs presented the best electrochemical response, which is essentially attributed to the suitable redox properties of Ce metal, acceptable level of biocompatibility, high electrical conductivity and large number of active and vacant sites for increasing enzyme loading. The biosensor displayed good sensitivity, a wide linear range, low LOD, satisfactory reproducibility and stability. In addition, this biosensor can be practically applied to determine paraoxon and other OPs in real samples. Because of these advantages, the Ce/UiO-66@MWCNTs layer is potentially suitable for immobilizing biological enzymes to develop electrochemical sensors for in–situ / in-field applications.

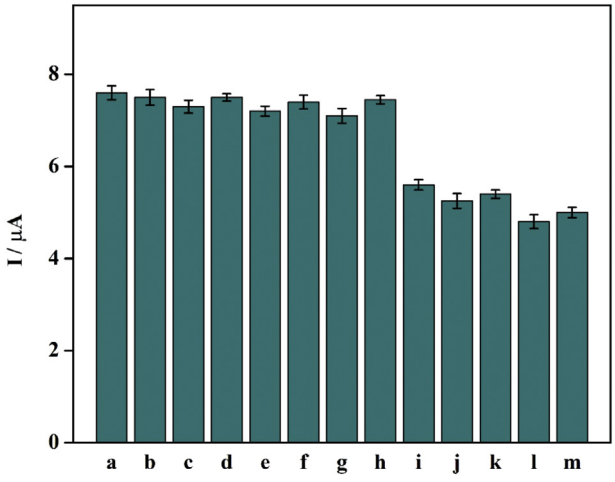


**Fig. 8.** DPV response in 0.1 M PBS containing 0.1 mM ATCl in the absence (a) and presence of 0.5 mM of oxalic acid(b), 3.5 mM of citric acid (c), 4 mM of glucose (d), 3 mM of $Mg^{2+}$ (e), 4 mM of $Fe^{3+}$ (f), 5 mM of $SO^{2-}$(g), 2.5 mM of $NO^{-}$(h), 10 nM of 4-Nitrophenol (i), 2 nM of carbaryl (j), 2 nM of carbofuran (k) 1.8 nM malathion (l) and 2 nM diazinon (m) after being incubated by 2 nM paraoxon for 12 min.

**Table 2**
Recovery studies for paraoxon in spinach and cabbage samples.

| Sample | Added (nM) | Found (nM) | RSD% ($n = 3$) | Recovery% |
|---|---|---|---|---|
| Spinach | 0 | 0 | 0 | – |
| | 10 | 10.2 | 3.2 | 102 |
| | 100 | 96 | 3.8 | 96 |
| Cabbage | 0 | 0 | 0 | – |
| | 10 | 9.5 | 4.1 | 95 |
| | 100 | 98.5 | 3.4 | 98.5 |

## Acknowledgments

The authors gratefully acknowledge the support provided by the Research Council of the Baqiyatallah University of Medical Sciences.

## References

[1] W. Zhang, A.M. Asiri, D. Liu, D. Du, Y. Lin, Nanomaterial-based biosensors for environmental and biological monitoring of organophosphorus pesticides and nerve agents, TrAC Trends Anal. Chem. 54 (2014) 1–10.
[2] M. Behl, J.-H. Hsieh, T.J. Shafer, W.R. Mundy, J.R. Rice, W.A. Boyd, et al., Use of alternative assays to identify and prioritize organophosphorus flame retardants for potential developmental and neurotoxicity, Neurotoxicol. Teratol. 52 (2015) 181–193.
[3] S. Qian, H. Lin, Colorimetric sensor array for detection and identification of organophosphorus and carbamate pesticides, Anal. Chem. 87 (2015) 5395–5400.
[4] Z. Cheng, F. Dong, J. Xu, X. Liu, X. Wu, Z. Chen, et al., Simultaneous determination of organophosphorus pesticides in fruits and vegetables using atmospheric pressure gas chromatography quadrupole-time-of-flight mass spectrometry, Food Chem. 231 (2017) 365–373.
[5] U.K. Priyadharshini, R. Latha, U. Kavitha, N. Nirmala, Effects of organophosphorus pesticides on cardiorespiratory parameters among the farmers, J. Clin. Diagn. Res. 11 (2017) CC01–CC04.
[6] G. Xue, Z. Yue, Z. Bing, T. Yiwei, L. Xiuying, L. Jianrong, Highly-sensitive organophosphorus pesticide biosensors based on CdTe quantum dots and bi-enzyme immobilized eggshell membranes, Analyst 141 (2016) 1105–1111.
[7] A.A. dos Santos, A.A. Naime, J. de Oliveira, D. Colle, D.B. dos Santos, M.A. Hort, et al., Long-term and low-dose malathion exposure causes cognitive impairment in adult mice: evidence of hippocampal mitochondrial dysfunction, astrogliosis and apoptotic events, Arch. Toxicol. 90 (2016) 647–660.
[8] E. Cequier, A.K. Sakhi, L.S. Haug, C. Thomsen, Exposure to organophosphorus pesticides in Norwegian mothers and their children: diurnal variability in concentrations of their biomarkers and associations with food consumption, Sci. Total Environ. 590 (2017) 655–662.
[9] K.H. Kim, E. Kabir, S.A. Jahan, Exposure to pesticides and the associated human health effects, Sci. Total Environ. 575 (2017) 525–535.
[10] R. Yu, Q. Liu, J. Liu, Q. Wang, Y. Wang, Concentrations of organophosphorus pesticides in fresh vegetables and related human health risk assessment in Changchun, Northeast China, Food Control 60 (2016) 353–360.
[11] R. Bala, R.K. Sharma, N. Wangoo, Development of gold nanoparticles-based aptasensor for the colorimetric detection of organophosphorus pesticide phorate, Anal. Bioanal. Chem. 408 (2016) 333–338.
[12] X. Yan, H. Li, X. Han, X. Su, A ratiometric fluorescent quantum dots based biosensor for organophosphorus pesticides detection by inner-filter effect, Biosens. Bioelectron. 74 (2015) 277–283.
[13] X. Hua, S.A. Eremin, F. Liu, M. Wang, Antibody developments and immunoassays for organophosphorus chemicals: a review, Curr. Org. Chem. 21 (2017) 2640–2652.
[14] J. Chen, W.-t. Zhang, Y. Shu, X.-h. Ma, X.-y. Cao, Detection of organophosphorus pesticide residues in leaf lettuce and cucumber through molecularly imprinted solid-phase extraction coupled to gas chromatography, Food Anal. Methods 10 (2017) 3452–3461.
[15] J.I. Cacho, N. Campillo, P. Vinas, M. Hernandez-Cordoba, In situ ionic liquid dispersive liquid-liquid microextraction coupled to gas chromatography-mass spectrometry for the determination of organophosphorus pesticides, J. Chromatogr. A 1559 (2018) 95–101.
[16] K. Seebunrueng, Y. Santaladchaiyakit, S. Srijaranai, Vortex-assisted low density solvent based demulsified dispersive liquid-liquid microextraction and high-performance liquid chromatography for the determination of organophosphorus pesticides in water samples, Chemosphere 103 (2014) 51–58.

[17] S.E. Hosseini, H. Saeidian, A. Amozadeh, M.T. Naseri, M. Babri, Fragmentation pathways and structural characterization of organophosphorus compounds related to the chemical weapons convention by electron ionization and electrospray ionization tandem mass spectrometry, Rapid Commun. Mass Spectrom. 30 (2016) 2585–2593.

[18] H. Ouyang, X. Tu, Z. Fu, W. Wang, S. Fu, C. Zhu, et al., Colorimetric and chemiluminescent dual-readout immunochromatographic assay for detection of pesticide residues utilizing g-C3N4/BiFeO3 nanocomposites, Biosens. Bioelectron. 106 (2018) 43–49.

[19] E.M. Brun, M. Garces-Garcia, R. Puchades, A. Maquieira, Enzyme-linked immunosorbent assay for the organophosphorus insecticide fenthion. Influence of hapten structure, J. Immunol. Methods 295 (2004) 21–35.

[20] G. Yang, X. Xu, M. Shen, W. Wang, L. Xu, G. Chen, et al., Determination of organophosphorus pesticides by capillary electrophoresis-inductively coupled plasma mass spectrometry with collective sample-introduction technique, Electrophoresis 30 (2009) 1718–1723.

[21] S. Boulanouar, S. Mezzache, A. Combes, V. Pichon, Molecularly imprinted polymers for the determination of organophosphorus pesticides in complex samples, Talanta 176 (2018) 465–478.

[22] Q. Liu, X. Jiang, Y. Zhang, L. Zheng, W. Jing, S. Liu, et al., A novel test strip for organophosphorus detection, Sensors Actuators B Chem. 210 (2015) 803–810.

[23] X. Yan, Y. Song, C. Zhu, H. Li, D. Du, X. Su, et al., MnO2 Nanosheet-carbon dots sensing platform for sensitive detection of organophosphorus pesticides, Anal. Chem. 90 (2018) 2618–2624.

[24] R. Thota, V. Ganesh, Selective and sensitive electrochemical detection of methyl parathion using chemically modified overhead projector sheets as flexible electrodes, Sensors Actuators B Chem. 227 (2016) 169–177.

[25] D. Song, Y. Wang, X. Lu, Y. Gao, Y. Li, F. Gao, Ag nanoparticles-decorated nitrogen-fluorine co-doped monolayer $MoS_2$ nanosheet for highly sensitive electrochemical sensing of organophosphorus pesticides, Sensors Actuators B Chem. 267 (2018) 5–13.

[26] F. Arduini, S. Cinti, V. Scognamiglio, D. Moscone, Nanomaterials in electrochemical biosensors for pesticide detection: advances and challenges in food analysis, Microchim. Acta 183 (2016) 2063–2083.

[27] J. Mehta, S. Dhaka, N. Bhardwaj, A.K. Paul, S. Dayananda, S. Lee, K.H. Kim, A. Deep, Application of an enzyme encapsulated metal-organic framework composite for convenient sensing and degradation of parathion, Sensors Actuators B Chem. 290 (2019) 267–274.

[28] N. Karimian, H. Fakhri, S. Amidi, A. Hajian, F. Arduini, H. Bagheri, A novel sensing layer based on metal-organic framework UiO-66 modified with $TiO_2$-graphene oxide: application to rapid, sensitive and simultaneous determination of paraoxon and chlorpyrifos, New J. Chem. 43 (2019) 2600–2609.

[29] X. Zhang, Y. Xu, B. Ye, An efficient electrochemical glucose sensor based on porous nickel-based metal-organic framework/carbon nanotubes composite (Ni-MOF/CNTs), J. Alloys Compd. 767 (2018) 651–656.

[30] J. Li, J. Xia, F. Zhang, Z. Wang, Q. Liu, An electrochemical sensor based on copper-based metal-organic frameworks-graphene composites for determination of dihydroxybenzene isomers in water, Talanta 181 (2018) 80–86.

[31] C. Li, R. Wu, J. Zou, T. Zhang, S. Zhang, Z. Zhang, et al., MNPs@ anionic MOFs/ERGO with the size selectivity for the electrochemical determination of H2O2 released from living cells, Biosens. Bioelectron. 116 (2018) 81–88.

[32] M. Deng, S. Lin, X. Bo, L. Guo, Simultaneous and sensitive electrochemical detection of dihydroxybenzene isomers with UiO-66 metal-organic framework/mesoporous carbon, Talanta 174 (2017) 527–538.

[33] J. Yang, L. Yang, H. Ye, F. Zhao, B. Zeng, Highly dispersed AuPd alloy nanoparticles immobilized on UiO-66-NH2 metal-organic framework for the detection of nitrite, Electrochim. Acta 219 (2016) 647–654.

[34] M. Lammert, C. Glißmann, N. Stock, Tuning the stability of bimetallic Ce (IV)/Zr (IV)-based MOFs with UiO-66 and MOF-808 structures, Dalton Trans. 46 (2017) 2425–2529.

[35] M. Kim, J.F. Cahill, H. Fei, K.A. Prather, S.M. Cohen, Postsynthetic ligand and cation exchange in robust metal-organic frameworks, J. Am. Chem. Soc. 134 (2012) 18082–18088.

[36] H.G.T. Nguyen, N.M. Schweitzer, C.-Y. Chang, T.L. Drake, M.C. So, P.C. Stair, et al., Vanadium-node-functionalized UiO-66: a thermally stable MOF-supported catalyst for the gas-phase oxidative dehydrogenation of cyclohexene, ACS Catal. 4 (2014) 2496–2500.

[37] S.J. Smith, B.P. Ladewig, A.J. Hill, C.H. Lau, M.R. Hill, Post-synthetic Ti exchanged UiO-66 metal-organic frameworks that deliver exceptional gas permeability in mixed matrix membranes, Sci. Rep. 5 (2015) 7823–7829.

[38] S. Dong, N. Li, T. Huang, H. Tang, J. Zheng, Myoglobin immobilized on LaF3 doped CeO2 and ionic liquid composite film for nitrite biosensor, Sensors Actuators B Chem. 173 (2012) 704–709.

[39] J. Fu, Q. Zhang, Z. Shi, Y. Guo, F. Li, Y. Zhang, et al., Sensitive acetylcholinesterase biosensor based on screen-printed carbon electrode modified with cerium oxide-chitosan/mesoporous carbon-chitosan for organophosphorus pesticide residue detection, Int. J. Electrochem. Sci. 13 (2018) 9231–9241.

[40] K.P. Kepp, A quantitative scale of Oxophilicity and Thiophilicity, Inorg. Chem. 55 (2016) 9461–9470.

[41] M. Hosseini, F.S. Sabet, H. Khabbaz, M. Aghazadeh, F. Mizani, M.R.J.A.M. Ganjali, Enhancement of the peroxidase-like activity of cerium-doped ferrite nanoparticles for colorimetric detection of H 2 O 2 and glucose, Anal. Methods 9 (2017) 3519–3524.

[42] T. Nagata, K. Miyajima, R.A. Hardy, G.F. Metha, F. Mafune, Reactivity of oxygen deficient cerium oxide clusters with small gaseous molecules, J. Phys. Chem. A 119 (2015) 5545–5552.

[43] H. Zhao, X. Ji, B. Wang, N. Wang, X. Li, R. Ni, et al., An ultra-sensitive acetylcholinesterase biosensor based on reduced graphene oxide-au nanoparticles-β-cyclodextrin/Prussian blue-chitosan nanocomposites for organophosphorus pesticides detection, Biosens. Bioelectron. 65 (2015) 23–30.

[44] M. Wen, X. Sun, L. Su, J. Shen, J. Li, S. Guo, The electrical conductivity of carbon nanotube/carbon black/polypropylene composites prepared through multistage stretching extrusion, Polymer 53 (2012) 1602–1610.

[45] J. Ding, Z. Yang, C. He, X. Tong, Y. Li, X. Niu, et al., UiO-66 (Zr) coupled with $Bi_2MoO_6$ as photocatalyst for visible-light promoted dye degradation, J. Colloid Interface Sci. 497 (2017) 126–133.

[46] Z. Yang, X. Xu, X. Liang, C. Lei, L. Gao, R. Hao, et al., Fabrication of Ce doped UiO-66/graphene nanocomposites with enhanced visible light driven photoactivity for reduction of nitroaromatic compounds, Appl. Surf. Sci. 420 (2017) 276–285.

[47] L. Valenzano, B. Civalleri, S. Chavan, S. Bordiga, M.H. Nilsen, S. Jakobsen, et al., Disclosing the complex structure of UiO-66 metal-organic framework: a synergic combination of experiment and theory, Chem. Mater. 23 (2011) 1700–1718.

[48] A.M. Ebrahim, T.J. Bandosz, Ce (III) doped Zr-based MOFs as excellent $NO_2$ adsorbents at ambient conditions, ACS Appl. Mater. Interfaces 5 (2013) 10565–10573.

[49] S. Abbasi, S.M. Zebarjad, S.H.N.J.E. Baghban, Decorating and Filling of Multi-Walled Carbon Nanotubes with $TiO_2$ Nanoparticles Via Wet Chemical Method, vol. 5, 2013 207–212.

[50] N. Hu, Z. Yang, Y. Wang, L. Zhang, Y. Wang, X. Huang, et al., Ultrafast and sensitive room temperature $NH_3$ gas sensors based on chemically reduced graphene oxide, Nanotechnology 25 (2014) 025502–025512.

[51] B. Gangar, K. Nagarajan, R. Venkata Krishnan, A. Pandit, Preparation of alumina and alumina-ceria microspheres using an internal gelation process and their characterization, Trans. Indian Ceram. Soc. 71 (2012) 101–109.

[52] T. dos Santos Pereira, G.C.M. de Oliveira, F.A. Santos, P.A. Raymundo-Pereira, O.N. Oliveira Jr., B.C. Janegitz, Use of zein microspheres to anchor carbon black and hemoglobin in electrochemical biosensors to detect hydrogen peroxide in cosmetic products, food and biological fluids, Talanta 194 (2019) 737–744.

[53] Y. Li, R. Zhao, L. Shi, G. Han, Y. Xiao, Acetylcholinesterase biosensor based on electrochemically inducing 3D graphene oxide network/multi-walled carbon nanotube composites for detection of pesticides, RSC Adv. 7 (2017) 53570–53577.

[54] N.K. Mogha, V. Sahu, M. Sharma, R.K. Sharma, D.T.J.M. Masram, Design, Biocompatible $ZrO_2$-reduced Graphene Oxide Immobilized AChE Biosensor for Chlorpyrifos Detection, vol. 111, 2016 312–320.

[55] H.B. Kaya, B. Ozcan, M. Sisecioglu, H. Ozdemir, Purification of acetylcholinesterase by 9-amino-1,2,3,4-tetrahydroacridine from human erythrocytes, Appl. Biochem. Biotechnol. 170 (2013) 198–209.

[56] Y. Jiang, X. Zhang, L. Pei, S. Yue, L. Ma, L. Zhou, et al., Silver nanoparticles modified two-dimensional transition metal carbides as nanocarriers to fabricate acetylcholinesterase-based electrochemical biosensor, Chem. Eng. J. 339 (2018) 547–556.

[57] W. Wei, S. Dong, G. Huang, Q. Xie, T. Huang, MOF-derived $Fe_2O_3$ nanoparticle embedded in porous carbon as electrode materials for two enzyme-based biosensors, Sensors Actuators B Chem. 260 (2018) 189–197.

[58] S. Wu, F. Huang, X. Lan, X. Wang, J. Wang, C.J.S. Meng, et al., Electrochemically Reduced Graphene Oxide and Nafion Nanocomposite for Ultralow Potential Detection of Organophosphate Pesticide, vol. 177, 2013 724–729.

[59] X. Lu, L. Tao, D. Song, Y. Li, F. Gao, Bimetallic Pd@ au nanorods based ultrasensitive acetylcholinesterase biosensor for determination of organophosphate pesticides, Sensors Actuators B Chem. 255 (2018) 2575–2581.

[60] L. Peng, S. Dong, W. Wei, X. Yuan, T. Huang, Synthesis of reticulated hollow spheres structure $NiCo_2S_4$ and its application in organophosphate pesticides biosensor, Biosens. Bioelectron. 92 (2017) 563–569.

[61] Q. Lang, L. Han, C. Hou, F. Wang, A. Liu, A sensitive acetylcholinesterase biosensor based on gold nanorods modified electrode for detection of organophosphate pesticide, Talanta 156-157 (2016) 34–41.

[62] G. Yu, W. Wu, Q. Zhao, X. Wei, Q. Lu, Efficient immobilization of acetylcholinesterase onto amino functionalized carbon nanotubes for the fabrication of high sensitive organophosphorus pesticides biosensors, Biosens. Bioelectron. 68 (2015) 288–294.

[63] H. Dzudzevic Cancar, S. Soylemez, Y. Akpinar, M. Kesik, S. Göker, G. Gunbas, et al., A novel acetylcholinesterase biosensor: core-shell magnetic nanoparticles incorporating a conjugated polymer for the detection of organophosphorus pesticides, ACS Appl. Mater. Interfaces 8 (2016) 8058–8067.

[64] R.R. Dutta, P. Puzari, Amperometric biosensing of organophosphate and organocarbamate pesticides utilizing polypyrrole entrapped acetylcholinesterase electrode, Biosens. Bioelectron. 52 (2014) 166–172.

[65] Y.P. Li, R.X. Zhao, G.Y. Han, Y.M. Xiao, Novel acetylcholinesterase biosensor for detection of Paraoxon based on holey graphene oxide modified glassy carbon electrode, Electroanalysis 30 (2018) 2258–2264.

[66] F. Zhao, Y. Yao, X. Li, L. Lan, C. Jiang, J.J.A.c. Ping, Metallic Transition Metal Dichalcogenide Nanosheets as an Effective and Biocompatible Transducer for Electrochemical Detection of Pesticide, vol. 90, 2018 11658–11664.

[67] J. Xu, C. Yu, T. Feng, M. Liu, F. Li, Y. Wang, et al., N-Carbamoylmaleimide-treated carbon dots: stabilizing the electrochemical intermediate and extending it for the ultrasensitive detection of organophosphate pesticides, Nanoscale 10 (2018) 19390–19398.

[68] N. Jha, S. Ramaprabhu, Development of au nanoparticles dispersed carbon nanotube-based biosensor for the detection of paraoxon, Nanoscale 2 (2010) 806–810.